Characterization of surface and subsurface defects induced by abrasive machining of optical crystals using grazing incidence X-ray diffraction and molecular dynamics

Yong Zhang [a], Qi Wang [a], Chen Li [a,*], Yinchuan Piao [a], Ning Hou [b], Kuangnan Hu [a]

[a] *School of Mechatronics Engineering, Harbin Institute of Technology, Harbin 150001, China*
[b] *School of Mechatronics Engineering, Shenyang Aerospace University, Shenyang 110136, China*

HIGHLIGHTS

- The mappings between micro cracks and diffraction pattern curves were revealed based on GIXD and MD.
- Surface and subsurface defects of CaF$_2$ crystals induced by abrasive machining were evaluated and characterized accurately.
- MD simulated results agreed well with the experimental results.
- This work provided a novel technology for nondestructive testing of defects of single crystals at nano- and micro- scales.

GRAPHICAL ABSTRACT
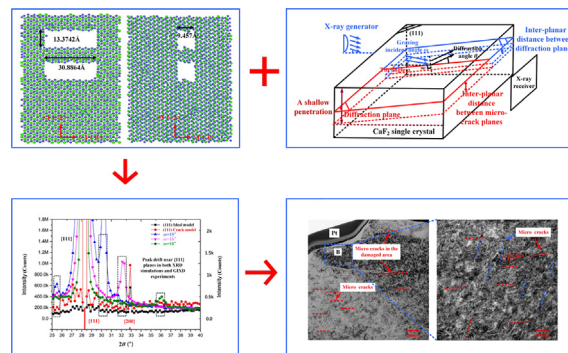
ARTICLE INFO

ABSTRACT

Introduction: Surface and subsurface defects were easily induced during abrasive machining process of optical crystals due to their high brittleness. Accurate characterization of these defects is the prerequisite for obtaining optical components with high surface integrity.
Objectives: This work aims to evaluate subsurface defects of CaF$_2$ single crystals induced by abrasive machining, the mappings between micro cracks and diffraction pattern curves, and the influence of micro cracks on lattice structures.
Methods: Molecular dynamics simulation, grazing incidence X-ray diffraction experiments and cross-sectional TEM detection were used in this work.
Results: In grazing incidence X-ray diffraction (GIXD) detection experiments on lapping and polished specimens, shifts phenomenon of the peak position under the non-theoretical grazing incidence angle indicated that the subsurface was damaged to a certain extent. The micro cracks of the subsurface were evaluated by the consistent characteristic of "peak drift" of the diffraction pattern curve in both experiments and simulations. In addition, cross-sectional TEM results showed that regular micro cracks were found on the subsurface, which agreed well with the simulation results.
Conclusion: The subsurface defects of CaF$_2$ single crystals induced by abrasive machining, and the influence of micro cracks on lattice structures can be evaluated by molecular dynamics simulation. The simulation results revealed the mappings between the micro cracks and diffraction pattern curve, which demonstrated that a

---

phenomenon of "peak drift" occurred near the diffraction angle of a specific crystal plane. This work provided a novel technology for the nondestructive testing of defects of single crystal materials at nano- and micro- scales.

Introduction

Optical crystals are conducive to produce high transmittance, high gain and low threshold, and are widely used in the fields of high-power lasers of multi-kW scale, lenses and prisms [1–4]. In recent years, many researchers have demonstrated strong interests in the growth of optical crystals with high quality and large size [5,6], performance characterization of optical crystals [7,8], service life of crystal components [9,10], etc. However, considerable studies acknowledged that surface and subsurface defects were easily induced during the machining process of optical materials due to their high brittleness, which could significantly affect the quality and service life of crystal devices [11–13]. To improve the surface integrity of optical components, many scholars have carried out lots of discussions on material removal [14,15] and damage generation [16,17] mechanisms, and parameter optimization during the machining progress [18,19].

It is the prerequisite for optimizing the process parameters to accurate characterization of surface and subsurface defects of optical components induced by abrasive machining. Many scholars did a lot of efforts to the defect characterization, which could be summarized in two aspects. One is non-destructive testing of the specimen through sound, heat, radiation and other mediums, such as high frequency scanning acoustic microscopy (HFSAM) [20], laser modulated scattering (LMS) [21] and enhanced internal reflection microscopy (EIRM) [22]. These non-destructive testing means take advantage of the physical properties of a certain aspect of the medium, and have a good effect on the defect analysis of specific materials. However, there are some shortcomings, such as low resolution, interference, and difficulty in modulating the signal. The other one is destructive testing means which refers to the local destruction of the specimen through some destructive methods. The damaged structure is exposed and then testing, such as chemical etching [23], cross-sectional microscopy [24], ball dimpling [25], angle polishing and magnetorheological polishing [26]. For destructive testing means, the preparation of the specimen is complicated and the evaluation range is limited. In addition, it is easy to induce the secondary damage to the specimen by using destructive testing means, which affects the detection accuracy of the experimental results. Therefore, it is of great significance to develop an efficient and accurate means to characterizing the defects of optical crystals induced by abrasive machining.

X-Ray diffraction (XRD) is an effective means for analyzing phase and evaluating crystal structure. Gay [27] et al. studied the dislocation structure of the metal surface after cold machining and annealing using XRD, and they established a theoretical model for analyzing the dislocation motion and estimated the dislocation density. Hordon [28] et al. developed a mathematical model for dislocation density matching of annealed and plastically strained Cu and Al single crystals based on XRD testing. They concluded that lattice tilting, localized bending, dislocation strain and sub-grain size represented important factors, which had distinct effects on broadening of diffraction lines. Nedjad [29] et al. studied the dislocation structure of massive martensite machined by electrochemical abrasive jet composite processing (EACJP) using XRD, and found that the processing parameters of EACJP had distinct effect on the density and distribution of screw dislocations. From the perspective of structural integrity, different types of defects represent obvious characteristics in the local lattice structure, and lead to the shift of the diffraction pattern curve, which result from properties of defects inherent in the lattice structure of the local regime. Therefore, XRD is particularly suitable for the non-destructive testing of defects of optical crystals. However, X-ray scattered on specimen surfaces is inevitably disturbed by the signals from the bulk when evaluating the subsurface structure of the specimen, which reduces the accuracy of experimental results. To solve the above problem, Hou [30] et al. used grazing incidence X-ray diffraction (GIXD) to detect the surface and subsurface defects induced during the ultra-precision machining process. They conducted X-ray incidence along a direction perpendicular to specific zone axis, which was approximately parallel to the specimen surface. Compared with the conventional XRD, GIXD enhanced the diffraction signal of specific crystal planes and avoided the signal interference from the bulk due to the shallow X-ray penetration depth. They carried out researches on the lattice misalignment structure (LMS) of the subsurface of KDP single crystal processed by ultra-precision machining. The characterization of LMS at varied depth was realized by controlling the grazing incidence angle, and the contents of LMS in the subsurface layer at different depths were revealed by the diffraction pattern curve.

Considerable researches showed that dislocations, micro-twins, stacking-faults, heavy-distorted lattices and micro cracks could be generated underneath the workpiece surface during the machining process of optical crystals [14–17]. Dislocation slip system plays a key role in the formation of defects, which leads to coupling defects in the surface and subsurface layers of the specimen. Although GIXD diffraction pattern curve could reveal defect contents in the subsurface layer, it is difficult to separate the characteristics of the defect and determine the specific defect type from the diffraction pattern curve. The present studies were lack to describe the lattice distortion caused by specific defect types from a microscopic viewpoint, especially the lack to establish the mappings between specific defect types and diffraction pattern characteristics of GIXD, which limited the application of GIXD in defect evaluation of optical crystals. As an effective simulation means, molecular dynamics (MD) has been widely used in microstructure evolution of the work materials during the indentation [31–33] and scratching [34–36] tests, by which the defects induced during the machining process such as dislocations, stacking faults and twins could be accurately predicted. It should be noted that some scholars have carried out XRD simulation with the aid of MD to analyze the physical properties of the crystals [37–42]. Coleman [37] et al. performed a research on the diffraction pattern curve of the grain boundary of Ni in XRD simulation of MD, in which virtual x-ray diffraction patterns directly from atomistic simulations was produced. This method could identify the misorientation of the grain boundary and show subtle differences between grain boundaries in the x-ray 2θ line profiles. Batyrev [38] et al. analyzed the structure of extended solids P3N5 under high pressure using MD simulation. A model with periodic boundary conditions consisting of 312,500 ions was generated, and the crystal orientation was random. The diffraction intensity of the model was simulated under the high pressure, and the results indicated that a new phase was generated induced by the high pressure. Then XRD detection experiments were performed to prove the accuracy of the simulated results of MD. Hawelek [39] et al. studied the transformation of ultra-dispersed diamond nanoparticles into carbon nano-onions by a combination of X-ray diffraction and molecular dynamics simulations. Two starting models consisting of 5460 and 13,500 atoms were relaxed, and pair correlation functions were compared with the experimental data. The simulated results agreed well with

the previous observations by high-resolution TEM. Müller [40] et al. studied the as-deposited structure of co-sputtered Cu-Ta alloys by X-ray diffraction coupled with molecular dynamics analysis. The amorphous structure was prepared from fcc and bcc initial lattices by a melt-quenching procedure, and then subsequently equilibrated for 5 ps. It was found that the XRD spectra of amorphous structures prepared by the melt-quenching procedure in MD were in good agreement with experimental results. Rosolankova [42] et al. measured the interplanar spacing of Cu crystals under shock compress using XRD simulation based on MD. A model with periodic boundary conditions was generated, and its orientations were [100], [010] and [001]. The diffraction intensity of the system was simulated, and the results showed that the diffraction intensity was plotted as a function normalized to the length of the [001] reciprocal lattice vector, which was in consistent with the experimental results. These studies [37–42] demonstrated that XRD simulation with the aid of MD was an effectively means to determine the mappings between specific type of defects and characteristics of the diffraction pattern curve.

In MD simulation, the potential between particles should be considered, and the crystal structure also has a significant influence on the simulation results. The relatively simple crystal structure is convenient for the introduction of defect model to analyze mappings between different defect types and diffraction pattern curves. CaF_2 single crystal is a typical optical crystal with a face-centered cubic structure. Many scholars have studied the microscopic properties of CaF_2 by means of MD simulation and achieved good results [43–46], which indicates that CaF_2 is suitable for studying the mappings between different defect types and diffraction pattern curves of optical crystals. Many researches performed MD simulation of CaF_2 crystals using Buckingham potential [31,44–47]. Lodes [31] et al. performed nanoindentation simulation of CaF_2 crystals using MD method, in which Buckingham potential was used. The simulated result showed that pop-in and size effect had distinct influence on the material deformation, and it agreed well with the experimental results, indicating that Buckingham potential was suitable for CaF_2 crystals. Gillan [45] et al. used Buckingham potential to simulate the entropy of formation of a point defect in CaF_2 crystals, and embedded crystalline and Green function methods were used in the damage lattice. The simulation results showed that the convergence of the calculated entropy was enhanced as the defect size increased, which agreed well with the experimental results. Morris [46] et al. analyzed the threshold displacement energy of CaF_2 crystals during the radiation damage process using MD simulation method, and found that F Frenkel pairs dominated CaF_2 damage. The above studies indicated that Buckingham potential can be used to perform the MD simulation of CaF_2 crystals in this work.

This work presented a new means using GIXD to evaluate the subsurface structure of optical crystals more precisely. The mappings between micro cracks and characteristics of the diffraction pattern curve of CaF_2 single crystals were systematically studied through both computational and experimental approaches. A model of the defect structure of micro cracks was established, and XRD simulation was performed with the aid of MD. In addition, lapping and polishing experiments of CaF_2 single crystals were performed, and detection experiments on the lapping and polished surface and subsurface of CaF_2 single crystals were performed by using GIXD technology. Finally, the simulation results were further verified by the TEM detection results.

Materials and methods

Potential of molecular dynamics

During the MD simulation process, the trajectories of all atoms in the system are calculated for a given period of time. The process

is accomplished by calculating interatomic forces based on gradients in their potential energy and solving Newton's equation of the motion for all atoms simultaneously. The results presented in this work were generated by MD LAMMPS codes [31].

The cleavage planes of CaF_2 single crystal are {111} planes, and the main slip planes at room temperature are {100} planes with ⟨110⟩ slip direction. To calculate the interaction between anions and cations, a potential is required, whose long-range Coulomb interaction needs to be considered. LAMMPS uses the particle–particle-grid method to calculate the Coulomb force with a cut-off radius of 10 Å [48]. The potential used in this work is given in Eq. (1).

$$V(r_{ij}) = \frac{1}{4\pi\varepsilon_0} \times \frac{Z_iZ_je^2}{r_{ij}} + A_{ij}e^{\left(-\frac{r_{ij}}{\rho_{ij}}\right)} - \frac{C_{ij}}{r_{ij}^6} \qquad (1)$$

A simulation of the same type has been used successfully for studying the plastic behavior in ionic crystals [32]. In the Buckingham potential, the energy U is a function of the distance r between ions A and B, their charges q, permittivity of vacuum ε_0 and three potential parameters A, ρ and C. The first long-range term describes the interaction between the ions, therefore, it is attractive to ions with a different charge sign and repulsive to ions with the same charge sign. The second short-range Born-Mayer term describes the repulsion caused by Pauli's law. The third term describes the attraction from the short-ranged van der Waals force. In general, nine potential parameters are needed to describe a system consisting of two types of ions. However, in the case of the CaF_2 crystal lattice for the doubly charged Ca^{2+} ions, only the strong Coulomb interaction is considered, whereas all other terms are neglected in this work [31,48]. Therefore, the free parameters are reduced to five parameters. The values of A, ρ, C for Ca-Ca are 0 eV, 1 Å and 0 eV/$Å^6$, respectively [31]. The values of A, ρ, C for Ca- F are 674.3 eV, 0 Å and 336 eV/$Å^6$, respectively [31]. The values of A, ρ, C for F-F are 1808 eV, 0.293 Å and 109.1 eV/$Å^6$, respectively [31].

To verify the potential, the static tensile simulations were carried out and the system deformation was uniformly increased along [100], [110] and [111] tensile axes. Fig. 1(a)–(c) present the three-dimensional view of three simulation models and their tensile axes. As shown in Fig. 1(d), the relevant elastic modulus was calculated from the stress-strain curve with a Poisson's ratio of 0.223. The simulated results of Elastic moduli for (100), (110) and (111) crystal planes were 121.4 GPa, 88.49 GPa and 80.1 GPa, respectively. The values of Elastic moduli for (100), (110) and (111) crystal planes were determined as 134 GPa, 119 GPa and 94 GPa, respectively [31]. It could be found that the simulation results agreed well with Ref. [31].

Micro crack models

Two models consisting of $8 \times 8 \times 8$ and $10 \times 10 \times 10$ unit cells were generated by using periodic boundary conditions [46,49,50], consisting of 36,864 ions and 12,000 ions, respectively. The crystal orientations of one model were [−110], [11−2] and [111] directions, whose length, width, and height were 61.77 Å, 106.99 Å, 75.66 Å, respectively. The crystal orientations of the other model were [100], [010] and [001] directions, whose length, width, and height were 54.6 Å, 54.6 Å, 54.6 Å, respectively. The NVE ensemble was selected to simulate the detection environment of GIXD experiment. The particle number (N), specimen volume (V), temperature (T), pressure (P) and energy (E) do not fluctuate and reach a stable state in GIXD experiment. The intensity of the diffraction pattern curve is closely related to the ion coordinates, so the motion state of the ions should be simulated as accurately as possible in the simulation process. Compared with those in
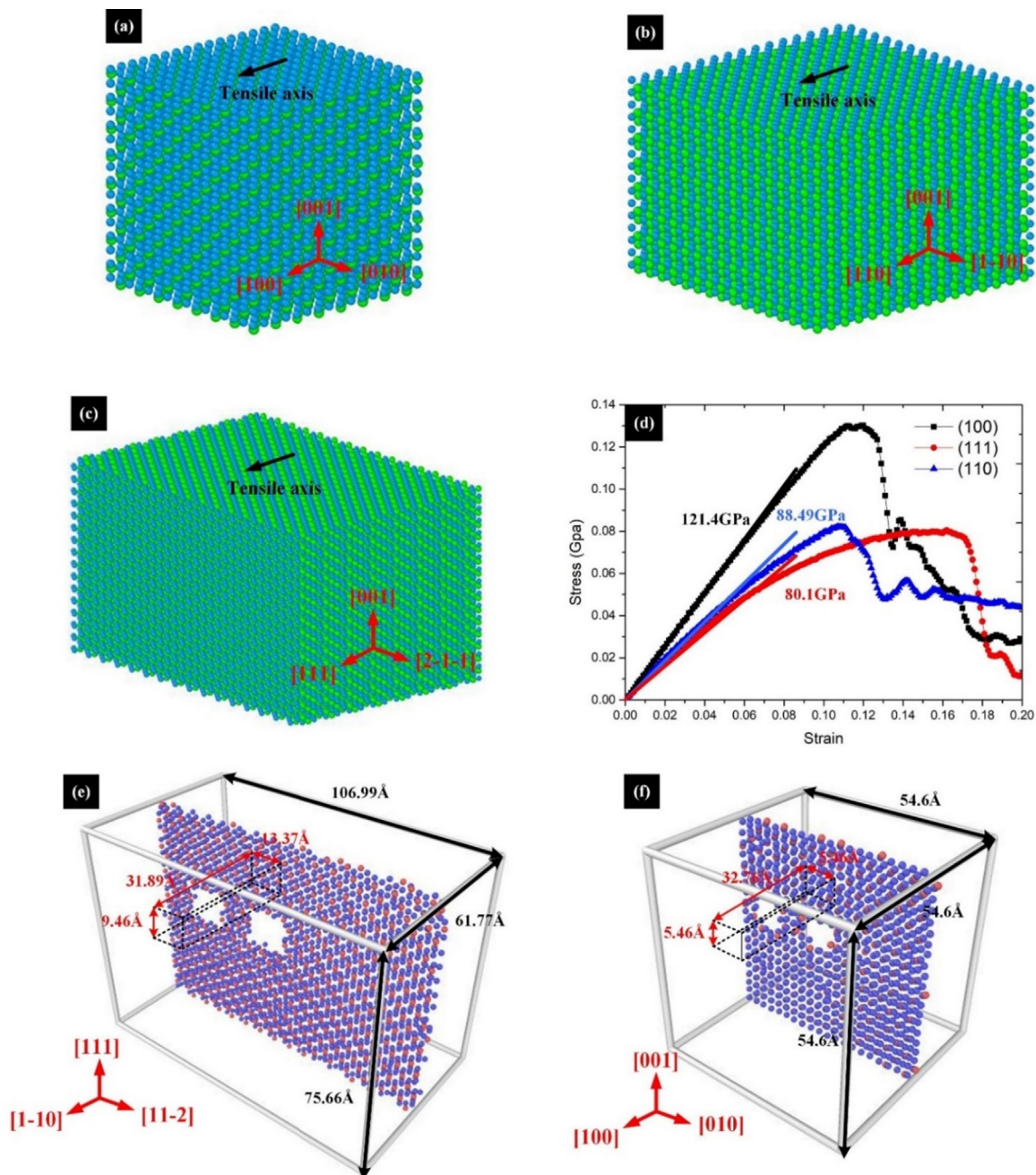
Fig. 1. Three simulations of static tensile along (a) [1 0 0] tensile axis, (b) [1 1 0] tensile axis and (c) [1 1 1] tensile axis, (d) simulated results of Elastic moduli for (1 0 0), (1 1 0) and (1 1 1) crystal planes, (e) (1 1 1) micro crack model and (f) (0 0 1) micro crack model.

NPT and NVT ensembles, the ions in NVE ensemble tend to be a freer state, which could ensure the accuracy of the simulation [31,32,50,51]. A starting temperature of 10^{-7} K was applied, and the time step was set to 10^{-15} s. The two models were marked with (1 1 1) ideal model and (0 0 1) ideal model, respectively.

The process of establishing micro cracks was divided into two steps. Firstly, the regimes of micro cracks in two ideal models were selected. In (1 1 1) micro crack model, the micro cracks were parallel to the (1 1 1) plane. Selected the cells from 3rd to 7th unit cell in [−1 1 0] direction, 1st to 2nd unit cell in [1 1 −2] direction, 3th to 4th unit cell in [1 1 −2] direction, 4th to 5th unit cell in [1 1 1] direction. In (0 0 1) micro crack model, the micro cracks were parallel to the (0 0 1) plane. Selected the cells from 2nd to 8th unit cell in [1 0 0] direction, 1st to 2nd unit cell in [0 1 0] direction, 3rd to 4th unit cell in [0 1 0] direction, 5th to 6th unit cell in [0 0 1] direction.

Finally, deleted the selected cells to construct the vacuum region. The system was then given the chance to relax for 20,000 fs in the NVE ensemble until fluctuations in potential energy and temperature decayed. Fig. 1(e) and (f) presents the three-dimensional view of micro crack models and their cross-sectional view.

XRD simulations

XRD simulation in LAMMPS used a simulated radiation of wavelength λ, and the diffraction intensity was calculated on a three-dimensional mesh of the reciprocal lattice nodes. The mesh size was defined by the entire simulation domain or the artificially selected regime [37]. The atomic scattering factors f_j resulted in the reduction in diffraction intensity due to Compton scattering. XRD simulation adopted analytical approximations of atomic scat-

tering factors which varied with the atomic type and diffraction angle. The analytic approximation was calculated using Eq. (2) [52].

$$f_j\left(\frac{sin(\theta)}{\lambda}\right) = \sum_i^4 a_i exp\left(-b_i \frac{sin^2(\theta)}{\lambda^2}\right) + c \tag{2}$$

This work used Cu as an incident radiation wavelength, which was 0.154 nm. Parameters a, b and c of Ca and F elements were determined by Ref. [53]. To study the influence of the micro crack model on the entire system, the entire simulation domain was selected and the polarization factor was introduced. The diffraction angle 2θ ranged from 20° to 90° with a fractional value of 0.2°. The models diffracted three times in total, with 1000 time-steps for one diffraction, and the corresponding diffraction pattern curves were fitted.

Experiment details

GIXD is a special diffraction mode in XRD. It is assumed that CaF$_2$ single crystal is a system composed of innumerable unit cells. Each cell is subjected to the stress during the machining process and rotates slightly in its original position. Mark cells in the same orientation with the same color. Fig. 2(a) shows the X-ray diffraction process of XRD. The crystal structure of X-ray could be characterized by the diffraction pattern curve at a certain penetration depth, but the signal interference from the bulk affects the experimental results. Fig. 2(b) shows the X-ray diffraction process of GIXD. The X-ray was incident along a direction perpendicular to the zone axis and was approximately parallel to the specimen, which enhances the diffraction signal of a specific crystal plane in the zone axis. The incident angle ω ensures a shallow penetration depth and reduces the interference from the bulk. The receiver collects the diffraction signal and characterizes the crystal structure details of a shallow penetration depth by controlling the grazing incident angle ω.

The specimens of CaF$_2$ single crystal used in this study were provided by Hefei Kejing Materials Technology co., LTD with a size of $10 \times 10 \times 1$ mm. The orientations of the crystal planes of the GaF$_2$ specimen were along [1−10], [11−2] and [111] zone axes. The lapping and polishing tests were carried out on the (111) surface by Al$_2$O$_3$ abrasive with the abrasive size of 14 μm and 1 μm, respectively. SEM of type SUPRA 55 SAPPHIRE was used to observe the surface morphology of the specimens. Fig. 3(b) and (c) show the surface morphologies of (111) lapping surface and (111) polished surface. It can be found that there were lots of defects on (111) lapping surface and almost no distinct defects on (111) polished surface. However, the defects of the specimen subsurface cannot be identified from the SEM images, and it is difficult to obtain a comprehensive evaluation of the processing quality of the specimen.

Compared with other nondestructive testing means, GIXD could avoid destroying the specimen and is more accurate and simpler. Therefore, GIXD was conducted to evaluate the subsurface defect of the specimens. To verify the accuracy of the simulated results, the characterization experiments of surface and subsurface defects were performed on an Empyrean X-ray diffractometer (PANalytical, Netherlands) with ceramic X-ray tubes and Cu radiation. Fig. 3(a) presents the experiment details of planes participating in diffraction of [1−10] zone axis. The specimen was placed with a definite orientation on diffractometer during the GIXD experiment. According to X-Ray diffraction crystallography, [1−10] zone axis is perpendicular to [111] and [11−2] zone axes, and parallel to [1−10] zone axis. Therefore, the X-ray was incident along a direction perpendicular to [1−10], and was approximately parallel to (111) plane during the GIXD experiment. A gasket with clear scale mark was placed under the specimen, and the specimen was rotated through the mark to ensure the position requirements. TEM of type TalosF200x was used to obtain a more intuitive evaluation on the defect structure of the specimen subsurface.

Results and discussion

Simulation results and discussion

Fig. 4(a) and (b) presented the whole diffraction pattern curve of the ideal model and micro crack model during the MD simulation with different time steps. The red line represents the relative diffraction intensity of each crystal plane in the standards of CaF$_2$ crystals. As shown in Fig. 4(a) and (b), the diffraction intensity in micro crack model decreased slightly compared with that in the ideal model during the XRD simulation. The position intensity of each crystal plane in (111) micro crack model and (001) micro crack model has almost no shifts, indicating that the micro crack can not affect the whole model.

To study the details of the diffraction pattern curve near the diffraction angle in (111) micro crack model, a local magnification of the whole diffraction pattern curve was obtained, as shown in Fig. 4(c). The diffraction peak in the blue dotted line is the phenomenon of peak position shift, which in accordance with the theoretical analysis. Under the condition of the same diffraction angle in the whole diffraction pattern curve, the diffraction peak intensity of the micro crack model was extremely high, while the diffraction peak intensity of the ideal model was extremely low. It was equivalent to the phenomenon of diffraction peak shift in micro crack model comparing with the ideal model, which was called "peak drift". Fig. 4(c) shows that the "peak drift" of micro crack model appears symmetrically near the diffraction angle of {111} planes, while the peak drift does not appear near the diffraction angle of other planes. The variation trends of the diffraction lines of (111) micro crack and (111) ideal models were almost
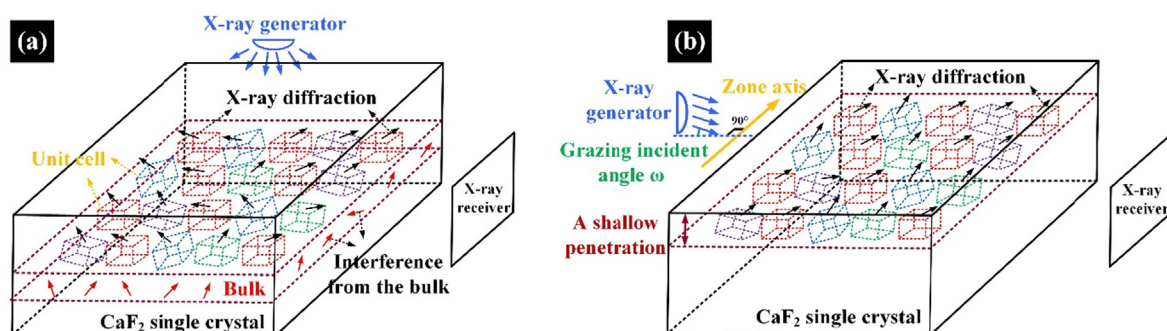

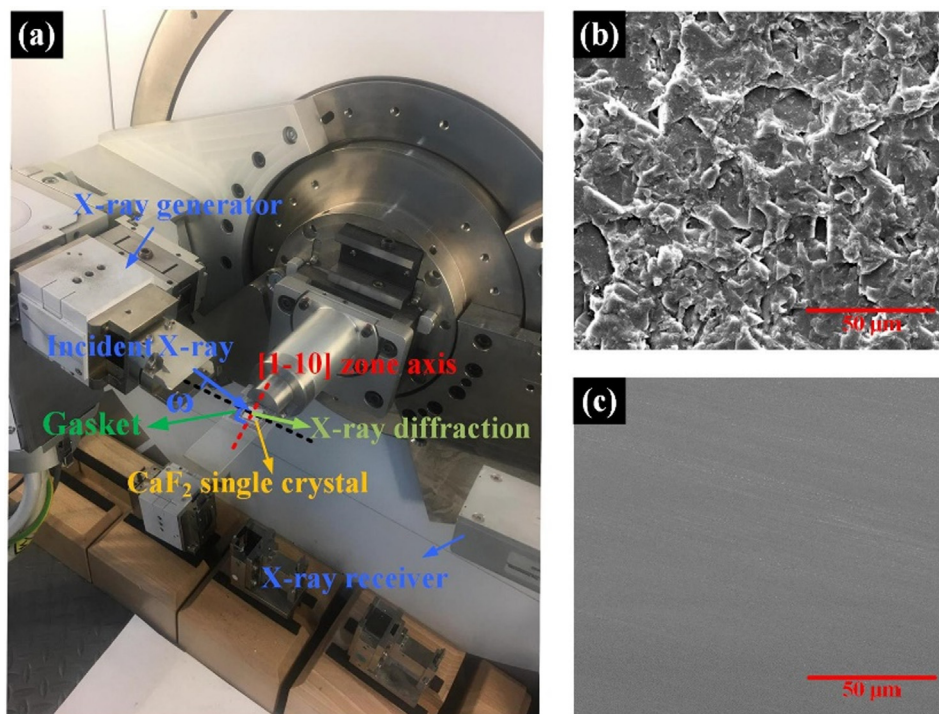**Fig. 2.** The schematic diagrams of X-ray diffraction process of (a) XRD and (b) GIXD.

Fig. 3. (a) The experiment details, and SEM images of morphologies of (b) (1 1 1) lapping surface and (c) (1 1 1) polished surface.
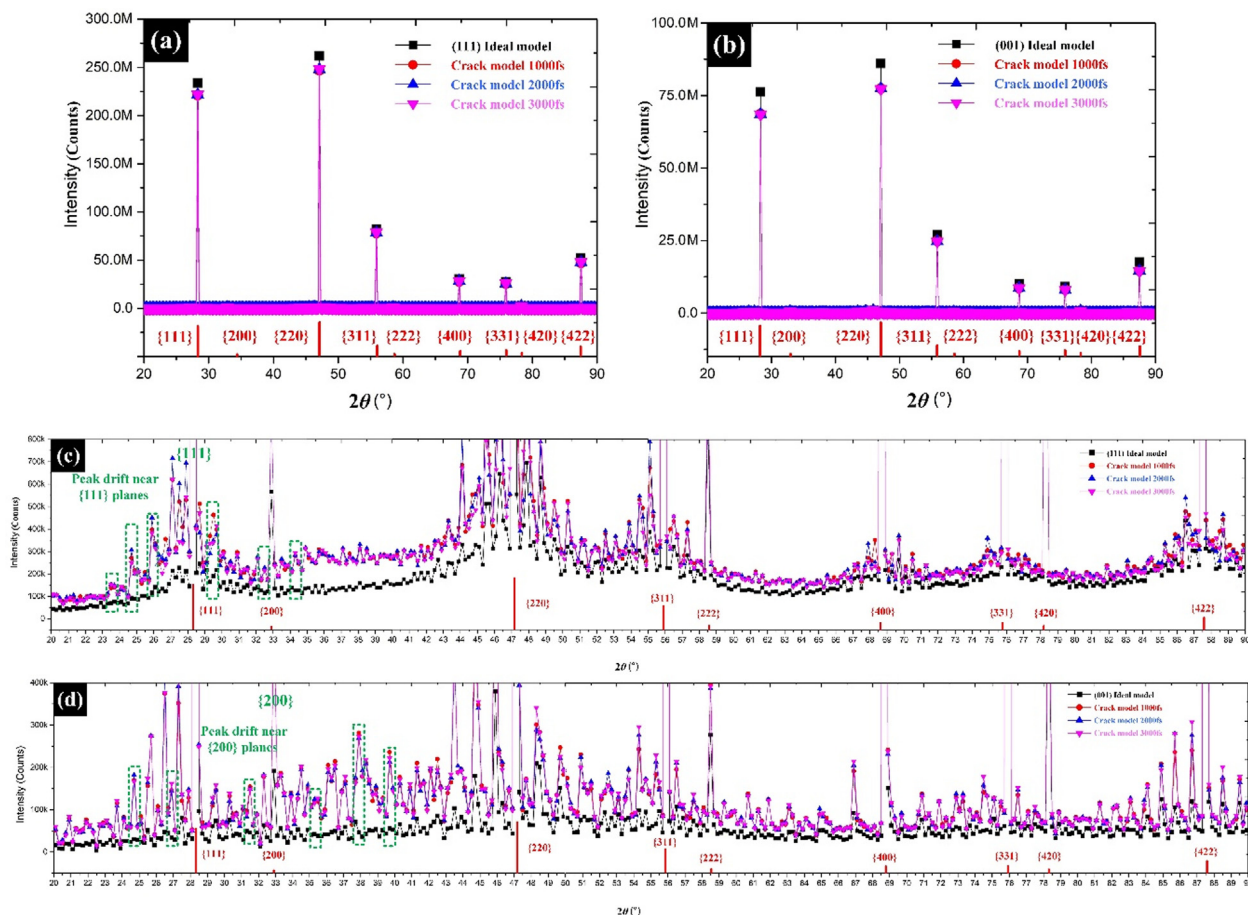

Fig. 4. The whole diffraction pattern curves of ideal and micro crack models during the MD simulation with different time steps on (a) (1 1 1) surface and (b) (0 0 1) surface, (c) local magnification of (a), and (d) local magnification of (b).
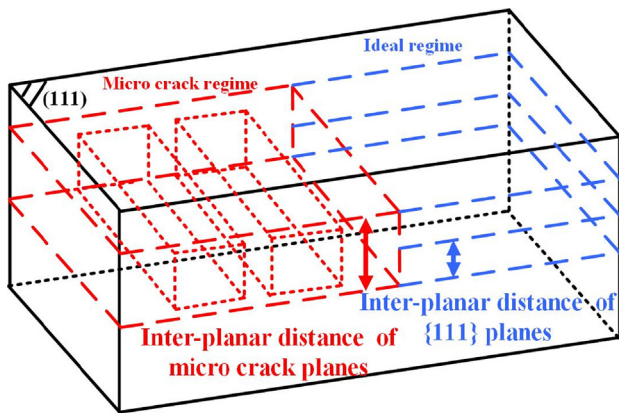
Fig. 5. Effect of the variation of local crystal structure induced by (111) micro crack model on inter-planar distance of {111} planes.

the same on the whole diffraction pattern curve except {111} planes, which was caused by micro cracks established in (111) micro crack model.

A similar diffraction law could be found in simulation of (001) micro crack model through the local magnification of the whole diffraction pattern curve, as shown in Fig. 4(d). The "peak drift" of the micro crack model appeared symmetrically near the diffraction angle of {200} planes in Fig. 4(d), while it did not appear near the diffraction angle of other planes. The diffraction peak corresponding to {100} planes was absent due to the extinction of

CaF$_2$ single crystals, which caused "peak drift" around the diffraction angle of {200} planes.

As shown in Fig. 5, the variation of the local crystal structure induced by the (111) micro crack model exhibited significant effect on the inter-planar distance of {111} planes, resulting in the shift of the diffraction pattern curve of {111} planes. The same law was also applicable to (001) micro crack model, resulting in the shift of the diffraction pattern curve of {200} planes. During the simulation process, micro cracks which were parallel to specific crystal plane corresponded to the "drift peak" of a specific crystal plane, which showed a strong mapping relationship.

The diffraction law of CaF$_2$ single crystal

Fig. 6(a) and (b) show the diffraction results of (111) lapping surface and (111) polished surface under different grazing incidence angles ω. As shown in Fig. 6(a), {420} planes could be found in the diffraction pattern curve of (111) polished surface under small grazing incidence angles. {111}, {220}, {331} and {420} planes could be found in the diffraction pattern curve of (111) lapping surface under identical grazing incidence angles, as shown in Fig. 6(b). When the X-ray was incident along a direction perpendicular to [1−10] zone axis, crystal planes in [1−10] zone axis were diffracted, resulting in diffraction peaks near the diffraction angle of corresponding crystal planes in the diffraction pattern curve, such as {111}, {220} and {311} planes. It should be noted that {420} plane did not belong to [1−10] zone axis, but the diffraction still occurred. In addition, the phenomenon of multi-peak diffraction appeared in the diffraction pattern curve of (111) lapping sur-
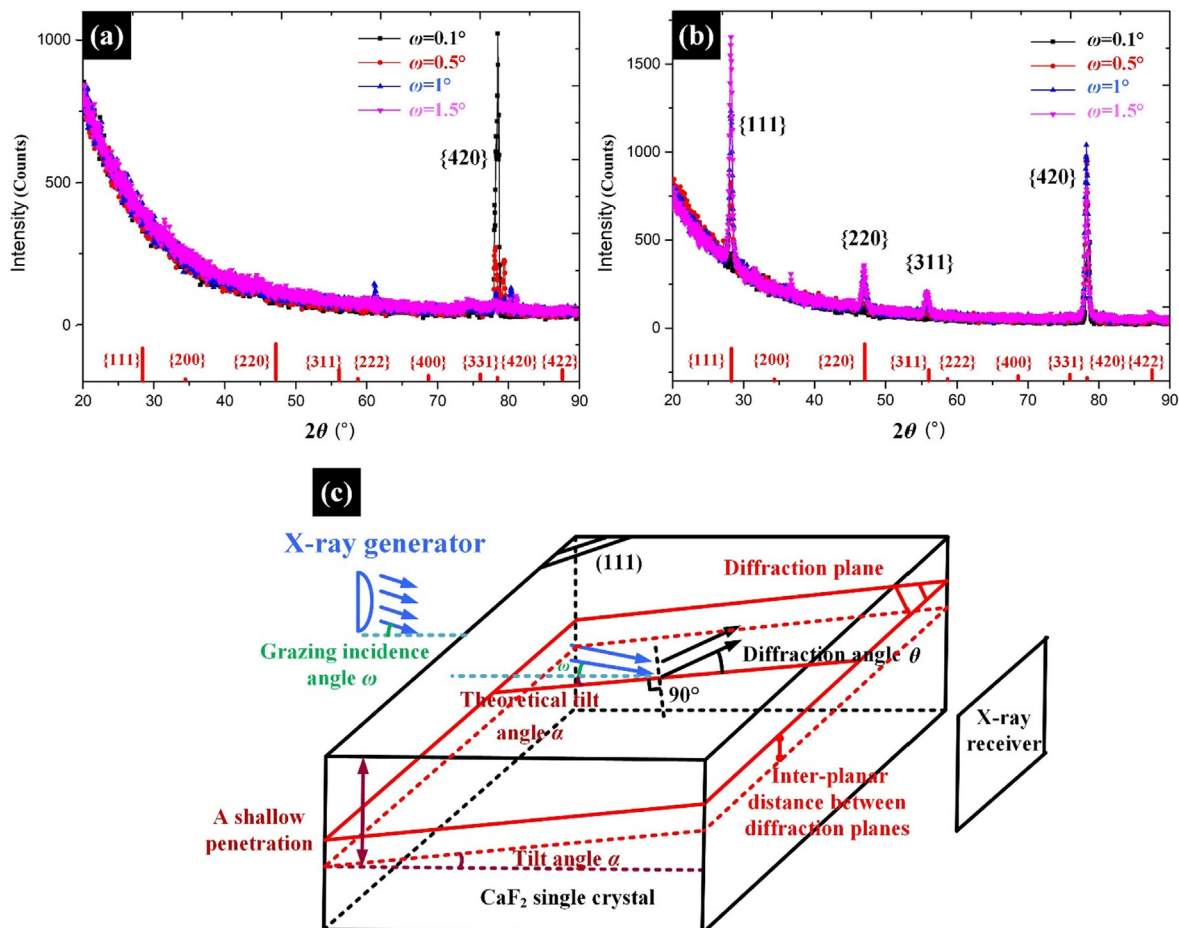

Fig. 6. Diffraction results of the specimen under small grazing incidence angles ω for (a) (111) polished surface and (b) (111) lapping surface, (c) geometric relationship among diffraction angle, X-ray grazing incidence angle and theoretical tilt angle of diffraction plane.

Table 1
Theoretical grazing incidence angles of each diffraction plane of CaF$_2$ single crystals.

Diffraction plane	Diffraction angle θ (°)	Tilt angle α (°)	Theoretical grazing incidence angle ω (°)
111	14.138	0	14.138
200	16.383	54.7356	—
220	23.508	35.2644	—
311	27.887	29.4962	—
222	29.244	0	29.244
400	34.340	54.7356	—
331	37.931	22.0017	15.9293
420	39.101	39.2315	—
422	43.70	19.4712	24.2288

face, which was different from the single-peak diffraction of the specific crystal plane under a specific grazing incidence angle. Therefore, the specimen subsurface seemed to be damaged to a certain extent, which led to obvious variations in the diffraction pattern curve.

It was assumed that all X-rays were incident from the left side of CaF$_2$ single crystals, the theoretical grazing incidence angle of X-ray was ω, and the diffraction angle of the specific plane was θ. There was a theoretical tilt angle α between the diffraction plane and the surface of CaF$_2$ crystals. The geometric relationship among the diffraction angle θ, X-ray grazing incidence angle ω and theoretical tilt angle α of the diffraction plane was shown in Fig. 6(c).

According to the geometric relationship in Fig. 6(c), the relative relationship among θ, ω and α could be calculated by Eq. (3). The theoretical grazing incidence angles of each diffraction crystal plane were calculated, as shown in Table 1.

$$\omega + \alpha = \theta \tag{3}$$

None of crystal planes could diffract under the small grazing incidence angle selected from Table 1. This results further indicated that the specimen subsurface was damaged to a certain extent after abrasive machining, resulting in the "peak drift" near the diffraction angle of a specific crystal plane in Fig. 6(c). It presented that GIXD could perform an intuitive and sensitive evaluation on the microstructure variations of the specimen.

The diffraction pattern curve of (111) polished surface and (111) lapping surface with more grazing incidence angles were shown in Fig. 7(a) and (b). It could be found that "peak drift" occurred near the diffraction angle of {111} planes in both polished and lapping surfaces under the grazing incidence angle near 14°, which agreed well with Table 1. The inter-planar distance d between {111} planes will be changed at the local regime due to the stress. In addition, the stress between {111} planes will be released when it reaches a certain extent, thus resulting in the formation of micro cracks in the subsurface. Fig. 7(c) presents the variation on the interplanar distance of {111} planes.

For simplifying the model, it was considered that the actual tilt angle between the diffraction plane and surface of CaF$_2$ crystals was identical to the theoretical tilt angle α in Eq. (3). Eq. (4) could be obtained from Eq. (3), which expressed the relationship between the grazing incidence angle ω with diffraction pattern curve.
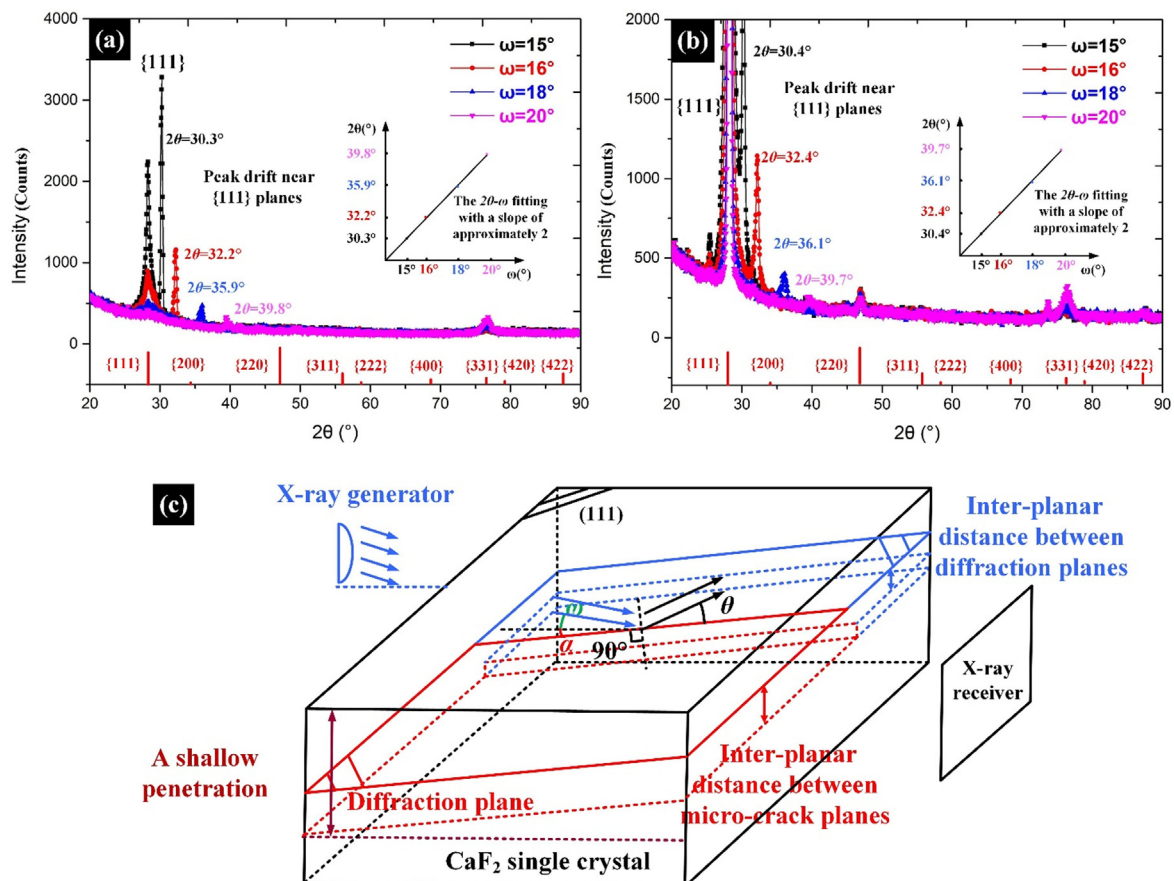
$$2\theta = 2\omega + 2\alpha \tag{4}$$

Fig. 7. The diffraction results of the specimen under more grazing incidence angles (a) (1 1 1) lapping surface (b) (1 1 1) polished surface, (c) variation on the interplanar distance of {1 1 1} planes.
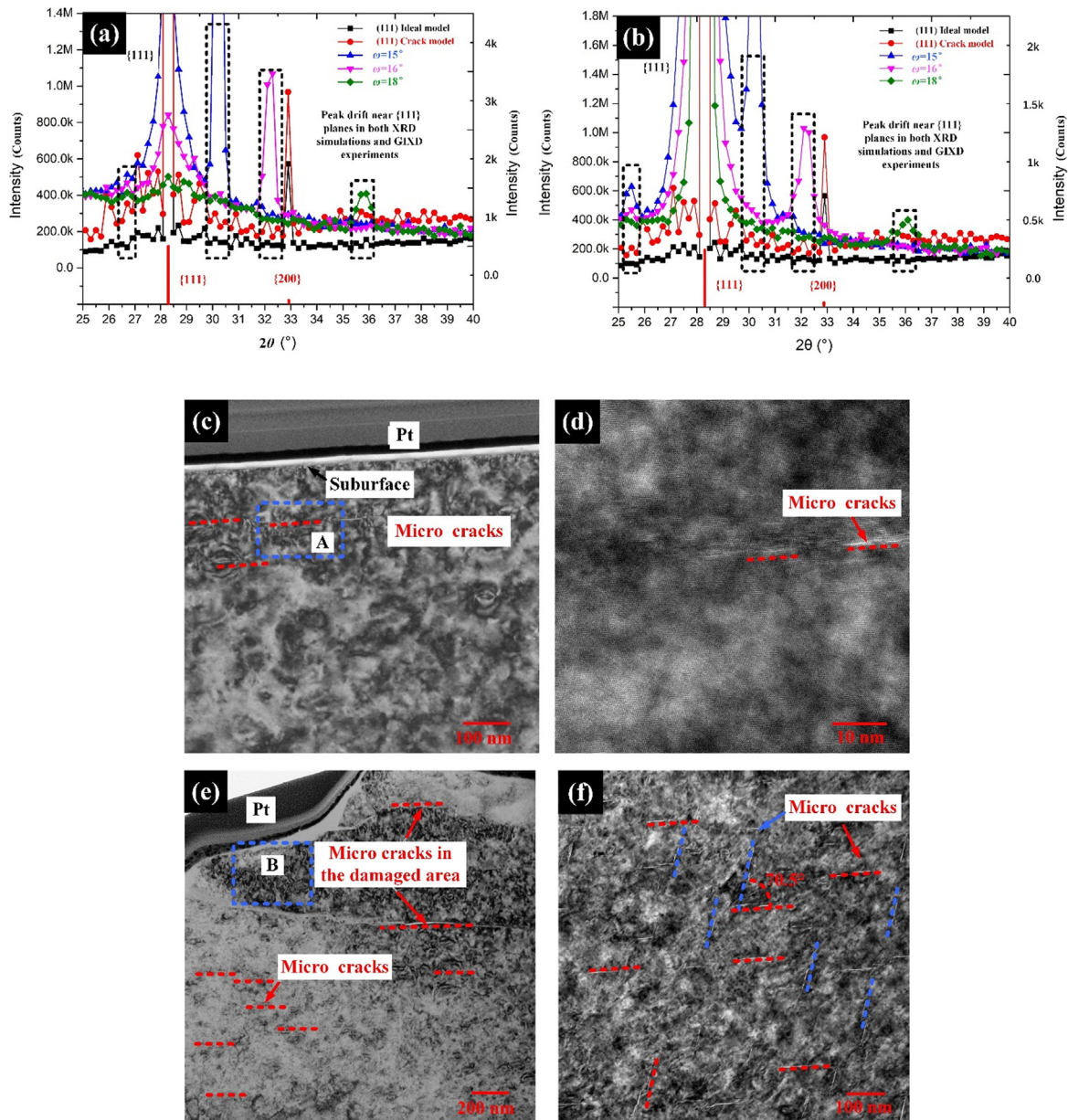
Fig. 8. Comparison of diffraction pattern curves near {1 1 1} planes between XRD simulation of micro crack model and GIXD experimental results on (1 1 1)-orientation (a) polished surface and (b) lapping surface, (c) TEM images of (1 1 1) polished subsurface, (d) HR-TEM images of region A in (c), (e) TEM images of (1 1 1) lapping subsurface and (f) Enlarged view of region B in (e).

From Eq. (4), it was found that there was a linear relationship between the diffraction angle 2θ and grazing incidence angle ω with a slope of 2. The 2θ-ω fitting of Fig. 7(a) and (b) was carried out, and a straight line with a slope of approximately 2 was obtained. When the inter-planar distance d between specific crystal planes varies, diffraction peaks would occur near the diffraction angle of the specific crystal plane under different grazing incidence angles, which was called "peak drift".

Verification results using GIXD and TEM

The comparison of diffraction pattern curves near {1 1 1} planes between XRD simulation results of (1 1 1) micro crack model and GIXD experimental results under different grazing incidence angles was shown in Fig. 8(a) and (b). It showed that diffraction angles of "drift peaks" in the simulation results agreed well with these in the experimental results, which indicated that there were micro cracks

parallel to {1 1 1} planes on both (1 1 1)-orientation polished and lapping subsurfaces.

Fig. 8(c) and (d) showed the TEM results of (1 1 1)-orientation polished subsurface. The results indicated that there were many micro cracks in the specimen subsurface, as shown in Fig. 8(c). The enlarged view of area A was shown in Fig. 8(d), from which micro cracks were found to be approximately parallel to the surface. In addition, no micro cracks could be found in the subsurface away from the surface, and damage layer depth was shallow during the polishing process.

Fig. 8(e) and (f) presented TEM images of (1 1 1)-orientation lapping subsurface. The results showed that there were many micro cracks in the lapping subsurface in Fig. 8(e), which were similar to (1 1 1) polished subsurface in Fig. 8(c). As shown in Fig. 8(f), the enlarged view of region B showed that there were many regular micro cracks with an angle of 70.5° to the surface. The included angle between the two {1 1 1} crystal planes was calculated as 70.5°, so the

regular micro cracks belonged to {1 1 1} planes. In addition, many micro cracks could be found in the subsurface, and the damage layer depth was deeper during the lapping process.

Conclusions

This paper proposed a theoretical study for evaluating the surface and subsurface defects of optical single crystals induced by abrasive machining based on molecular dynamics simulation and grazing incidence X-ray diffraction. The following conclusions can be drawn:

MD simulation model of micro cracks in CaF_2 single crystals was established, and the mappings between the XRD diffraction pattern curve and micro cracks were analyzed. The results indicated that a phenomenon of "peak drift" occurred near the diffraction angle of a specific crystal plane in the XRD diffraction pattern curve of micro-crack simulation model.

GIXD experiments of subsurface defects of CaF_2 single crystals after abrasive machining were performed. Micro cracks in the specimen subsurface were evaluated by the consistent characteristic of "peak drift" of the diffraction pattern curve in GIXD detection experiment and XRD simulation.

Finally, the subsurface defects of CaF_2 single crystals processed by lapping and polishing were analyzed with the aid of cross-sectional TEM experiments. The results showed that many regular micro cracks which were parallel to or at certain angles to the specimen surface, which agreed well with the simulation results. The TEM results can further prove the accuracy of the specific law of this work. This work provided a novel technology for the nondestructive testing of defects of single crystal materials at nano- and micro-scales.

Compliance with Ethics Requirements

This article does not contain any study with human or animal subjects.

CRediT authorship contribution statement

Yong Zhang: Writing - review & editing. **Qi Wang:** Writing - original draft, Data curation. **Chen Li:** Writing - review & editing. **Yinchuan Piao:** Writing - review & editing. **Ning Hou:** Writing - review & editing. **Kuangnan Hu:** Writing - review & editing.

Declaration of Competing Interest

The authors declare that they have no known competing financial interests or personal relationships that could have appeared to influence the work reported in this paper.

Acknowledgment

References

[1] Fleurot N, Cavailler C, Bourgade JL. The Laser Megajoule (LMJ) Project dedicated to inertial confinement fusion: development and construction status. Fusion Eng Des 2005;74(1–4):147–54.

[2] Xu J, Kang R, Dong Z, Wang Z. Review of chemical mechanical polishing of silicon wafers. Diamond Abrasive Eng 2020;238(4):24–33.

[3] Li C, Zhang F, Wu Y, Zhang X. Influence of strain rate effect on material removal and deformation mechanism based on ductile nanoscratch tests of Lu_2O_3 single crystal. Ceram Int 2018;44(17):21486–98.

[4] Chen N, Li HN, Wu J, Li Z, Li L, Liu G, et al. Advances in micro milling: From tool fabrication to process outcomes. Int J Mach Tools Manuf 2021;160:103670.

[5] Li Y, Yuan Z, Wang J, Xu Q. Laser-induced damage characteristics in fused silica surface due to mechanical and chemical defects during manufacturing processes. Opt Laser Technol 2017;91:149–58.

[6] Ye H, Li Y, Yuan Z, Wang J, Yang W, Xu Q. Laser induced damage characteristics of fused silica optics treated by wet chemical processes. Appl Surf Sci 2015;357:498–505.

[7] Liu H, Ye X, Zhou X, Huang J, Wang F, Zhou X, et al. Subsurface defects characterization and laser damage performance of fused silica optics during HF-etched process. Opt Mater 2014;36(5):855–60.

[8] Li C, Zhang F, Zhou G, Wei Z, Zhang L. Theoretical modelling of brittle-to-ductile transition load of KDP crystals on (001) plane during nanoindentation and nanoscratch tests. J Mater Res Technol 2020;9(6):14142–57.

[9] Taheri N, Naffakh-Moosavy H, Ghaini FM. A new procedure for refurbishment of power plant Superalloy 617 by pulsed Nd: YAG laser process. Opt Laser Technol 2017;91:71–9.

[10] Choubey A, Jain RK, Ali S, Singh R, Vishwakarma SC, Agrawal DK, et al. Studies on pulsed Nd: YAG laser cutting of thick stainless steel in dry air and underwater environment for dismantling applications. Opt Laser Technol 2015;71:6–15.

[11] Meng B, Zhang Y, Zhang F. Material removal mechanism of 6H-SiC studied by nano-scratching with Berkovich indenter. Appl Phys A 2016;122(3):247.

[12] Li C, Zhang F, Meng B, Rao X, Zhou Y. Research of material removal and deformation mechanism for single crystal GGG ($Gd_3Ga_5O_{12}$) based on varied-depth nanoscratch testing. Mater Des 2017;125:180–8.

[13] Li C, Li X, Huang S, Li L, Zhang F. Ultra-precision grinding of $Gd_3Ga_5O_{12}$ crystals with graphene oxide coolant: Material deformation mechanism and performance evaluation. J Manuf Processes 2021;61:417–27.

[14] Zhang Y, Hou N, Zhang LC. Investigation into the room temperature creep-deformation of potassium dihydrogen phosphate crystals using nanoindentation. Adv Manuf 2018;6(4):376–83.

[15] Wang H, Riemer O, Rickens K, Brinksmeier E. On the mechanism of asymmetric ductile–brittle transition in microcutting of (111) CaF_2 single crystals. Scr Mater 2016;114:21–6.

[16] Li C, Wu Y, Li X, Ma L, Zhang F, Huang H. Deformation characteristics and surface generation modelling of crack-free grinding of GGG single crystals. J Mater Process Technol 2020;279:116577.

[17] Li C, Li X, Wu Y, Zhang F, Huang H. Deformation mechanism and force modelling of the grinding of YAG single crystals. Int J Mach Tools Manuf 2019;143:23–37.

[18] Li C, Zhang F, Meng B, Liu L, Rao X. Material removal mechanism and grinding force modelling of ultrasonic vibration assisted grinding for SiC ceramics. Ceram Int 2017;43(3):2981–93.

[19] Hou N, Zhang L, Zhang Y, Zhang F. On the ultra-precision fabrication of damage-free optical KDP components: mechanisms and problems. Crit Rev Solid State Mater Sci 2019;44(4):283–97.

[20] Rats D, Von Stebut J, Augereau F. High frequency scanning acoustic microscopy: a novel non-destructive surface analytical tool for assessment of coating-specific elastic moduli and tomographic study of subsurface defects. Thin Solid Films 1999;355:347–52.

[21] Wu ZL, Sheehan L, Kozlowski MR. Laser modulated scattering as a nondestructive evaluation tool for defect inspection in optical materials for high power laser applications. Opt Express 1998;3(10):376–83.

[22] Xu L, Ni K, Zhu R, Liu X, Liu S, Zhang B, et al. Enhanced internal reflection microscopy for subsurface damage inspection. In: Pacific Rim Laser Damage 2016: Optical Materials for High-Power Lasers, vol. 9983. International Society for Optics and Photonics, July; 2016. p. 99830Z.

[23] Huang Z, Geyer N, Werner P, De Boor J, Gösele U. Metal-assisted chemical etching of silicon: a review: in memory of Prof. Ulrich Gösele. Adv Mater 2011;23(2):285–308.

[24] Ouattara L, Ulloa JM, Mikkelsen A, Lundgren E, Koenraad PM, Borgström M, et al. Correlation lengths in stacked InAs quantum dot systems studied by cross-sectional scanning tunnelling microscopy. Nanotechnology 2007;18 (14):145403.

[25] Guillet F, Bertussi B, Lamaignere L, Leborgne X, Minot B. Preliminary results on mitigation of KDP surface damage using the ball dimpling method. In: Laser-induced damage in optical materials: 2007, vol. 6720. International Society for Optics and Photonics, December; 2007. p. 672008.

[26] Menapace JA, Davis PJ, Steele WA, Wong LL, Suratwala TI, Miller PE. MRF applications: measurement of process-dependent subsurface damage in optical materials using the MRF wedge technique. In: Laser-induced damage in optical materials: 2005, vol. 5991. International Society for Optics and Photonics, February; 2006. p. 599103.

[27] Gay P, Hirsch PB, Kelly A. The estimation of dislocation densities in metals from X-ray data. Acta Metall 1953;1(3):315–9.

[28] Hordon MJ, Averbach BL. X-ray measurements of dislocation density in deformed copper and aluminum single crystals. Acta Metall 1961;9 (3):237–46.

[29] Nedjad SH, Nasab FH, Garabagh MM, Damadi SR, Ahmadabadi MN. X-ray diffraction study on the strain anisotropy and dislocation structure of deformed lath martensite. Metall Mater Trans A 2011;42(8):2493–7.

[30] Hou N, Zhang Y, Zhang L, Zhang F. Assessing microstructure changes in potassium dihydrogen phosphate crystals induced by mechanical stresses. Scr Mater 2016;113:48–50.

[31] Lodes MA, Hartmaier A, Göken M, Durst K. Influence of dislocation density on the pop-in behavior and indentation size effect in CaF_2 single crystals: experiments and molecular dynamics simulations. Acta Mater 2011;59 (11):4264–73.

[32] Armstrong P, Knieke C, Mackovic M, Frank G, Hartmaier A, Göken M, et al. Microstructural evolution during deformation of tin dioxide nanoparticles in a comminution process. Acta Mater 2009;57(10):3060–71.

[33] Chua J, Zhang R, Chaudhari A, Vachhani SJ, Kumar AS, Tu Q, et al. High-temperature nanoindentation size effect in fluorite material. Int J Mech Sci 2019;159:459–66.

[34] Xiao G, He Y, Geng Y, Yan Y, Ren M. Molecular dynamics and experimental study on comparison between static and dynamic ploughing lithography of single crystal copper. Appl Surf Sci 2019;463:96–104.

[35] Yan Y, He Y, Xiao G, Geng Y, Ren M. Effects of diamond tip orientation on the dynamic ploughing lithography of single crystal copper. Precis Eng 2019;57:127–36.

[36] Yan Y, Li Z, Jia J, Wang J, Geng Y. Molecular dynamics simulation of the combination effect of the tip inclination and scratching direction on nanomachining of single crystal silicon. Comput Mater Sci 2013;186:110014.

[37] Coleman SP, Spearot DE, Capolungo L. Virtual diffraction analysis of Ni [0 1 0] symmetric tilt grain boundaries. Modell Simul Mater Sci Eng 2013;21 (5):055020.

[38] Batyrev IG, Coleman SP, Ciezak-Jenkins JA, Stavrou E, Zaug JM. Modeling and measurements of the XRD patterns of extended solids under high-pressure. AIP Conf Proc 2018;1979:050003.

[39] Hawelek L, Brodka A, Tomita S, Dore JC, Honkimäki V, Burian A. Transformation of nano-diamonds to carbon nano-onions studied by X-ray diffraction and molecular dynamics. Diam Relat Mater 2011;20(10):1333–9.

[40] Müller CM, Parviainen S, Djurabekova F, Nordlund K, Spolenak R. The as-deposited structure of co-sputtered Cu-Ta alloys, studied by X-ray diffraction and molecular dynamics simulations. Acta Mater 2015;82:51–63.

[41] Kimminau G, Nagler B, Higginbotham A, Murphy WJ, Park N, Hawreliak J, et al. Simulating picosecond x-ray diffraction from shocked crystals using post-processing molecular dynamics calculations. J Phys: Condens Matter 2008;20 (50):505203.

[42] Rosolankova K, Kalantar DH, Belak JF, Bringa EM, Caturla MJ, Hawreliak J, et al. X-ray diffraction from shocked crystals: experiments and predictions of molecular dynamics simulations. AIP Conf Proc 2004;706:1195–8.

[43] Sun XW, Chu YD, Liu ZJ, Chen QF, Song Q, Song T. Simulated equation of state of CaF_2 with fluorite-type structure at high temperature and high pressure. Physica B 2009;404(1):158–62.

[44] Evangelakis GA, Pontikis V. Fast-ion conduction in fluorite CaF_2 studied by equilibrium and nonequilibrium molecular dynamics. Phys Rev B 1991;43 (4):3180–7.

[45] Gillan MJ, Jacobs PWM. Entropy of a point defect in an ionic crystal. Phys Rev B 1983;28(2):759–77.

[46] Morris J, Cowen BJ, Teysseyre S, Hecht AA. Molecular dynamics investigation of threshold displacement energies in CaF_2. Comput Mater Sci 2020;172:109293.

[47] Evangelakis GA, Pontikis V. Direct computation of the superionic conductivity in CaF_2 by constant-temperature equilibrium and nonequilibrium molecular dynamics. Europhys Lett 1989;8(7):599–604.

[48] Jin QH, Feng SS, Guo ZY, Li BH, Ding DT. Calculations of the formation energies of point defects in alkaline earth fluorides. Acta Phys Sin 1999;48(7):1261–8.

[49] Zhao S, Germann TC, Strachan A. Molecular dynamics simulation of dynamical response of perfect and porous Ni/Al nanolaminates under shock loading. Phys Rev B 2007;76(1):014103.

[50] Chuklina N, Mysovsky A. Theoretical study of self-trapped hole diffusion in CaF_2, SrF_2, BaF_2 crystals. Radiat Meas 2019;128:106135.

[51] Baskurt M, Kang J, Sahin H. Octahedrally coordinated single layered CaF_2: robust insulating behaviour. PCCP 2020;22(5):2949–54.

[52] Hahn T, Shmueli U, Arthur JW. International tables for crystallography. Dordrecht: Reidel; 1983.

[53] Peng LM, Ren G, Dudarev SL, Whelan MJ. Robust parameterization of elastic and absorptive electron atomic scattering factors. Acta Crystallogr A 1996;52 (2):257–76.